IECB 2022

MDPI

Proceedings

Aptamer functionalisation of back-gated graphene field effect transistors for Pb^{2+} sensing

Benjamin O'Driscoll[1*], Vikram Srinivasa Raghavan[2], Theodore Bungon[1], Paul Davey[1], Toby Whitley[1], Shakil A. Awan[1] and Sai Siva Gorthi[2].

[1] Wolfson Nanomaterials & Devices Laboratory, School of Engineering, Computing and Mathematics, University of Plymouth, Plymouth, Devon, *PL4 8AA, UK*; theodore.bungon@plymouth.ac.uk (T.B); paul.davey@plymouth.ac.uk (P.D.); toby.whitley@plymouth.ac.uk (T.W.); shakil.awan@plymouth.ac.uk (S.A.A)

[2] Optics and Microfluidics Instrumentation Lab, Department of Instrumentation and Applied Physics, Indian Institute of Science, Bangalore 560012, India.; vikrams@iisc.ac.in (V.S.R); saisiva@iisc.ac.in (S.S.G)

* Correspondence: benjamin.odriscoll@plymouth.ac.uk (B.O.D)

† Presented at the 2nd International Electronic Conference on Biosensors, 14-18 February 2022.

Abstract: We discuss the development of aptamer functionalized, back-gated, graphene field effect transistor (GFET) biosensors for the targeted detection of Lead (Pb^{2+}) ions. The widespread existence of the heavy metal Pb^{2+} in the environment is a severe threat to the health of humans. It is a neurotoxin that accumulates over time in the body restricting the cognitive, behavioral and psychological development of children along with causing irreversible harm to the human fetus. New biosensors which allow for the rapid, sensitive and low-cost detection of Pb^{2+} are required to monitor this toxicant in water sources worldwide. The GFET devices were fabricated using a scalable photolithographic patterning process with evaporated Cr and sputtered Au contacts over monolayer graphene on Si/SiO_2. The single stranded Thrombin Binding Aptamer (TBA) was immobilized onto the graphene channel either directly with a pyrene terminated 5′ end or indirectly using the 1-pyrenebutanoic acid succinimidyl ester (PBASE) molecule to facilitate DNA crosslinking with an amine modified 5′ end. Herein provides an evaluation of these two immobilization strategies for the detection of Pb^{2+}. Functionalized states were verified using Raman spectroscopy and electrically characterized using 4-probe electrical measurements to determine transfer curves allowing the calculation of field effect mobility and Dirac Point characteristics.

Keywords: Graphene; GFET; Lead; Aptamer; Thrombin Binding Aptamer (TBA); G-quadruplex;

Citation: O'Driscoll, B.; Raghavan, V.S..; Bungon, T.; Davey, P.; Whitley, T.; Awan, S.A.; Gorthi, S.S. Aptamer functionalisation of back-gated graphene field effect transistors for Pb2+ sensing. *Eng. Proc.* **2021**, *3*, x. https://doi.org/10.3390/xxxxx

Published: date

1. Introduction

Research groups the world over have been fascinated with graphene based research ever since its discovery in 2004 [1]. In particular it offers a plethora of advantageous electronic properties over Si based devices for biosensing technologies including high mobility [2], sensitivity and biocompatibility [3]. Graphene is a two-dimensional allotrope of sp^2 hybridized Carbon and therefore offers a large surface area to volume ratio making it particularly sensitive to its surroundings, a characteristic that has engaged research groups keen to exploit this for biosensing technologies. One common application of this material as a biosensor is in graphene field effect transistors (GFETs) [4, 5]. GFETs are realized by connecting a conducting graphene channel between metal source and drain electrodes, achieved in either the top- [6] or back-gated [7] configuration. These biosensors replace the doped Si channel in traditional FETs with graphene which is subsequently functionalized with bioreceptors to target specific analytes.

Graphene is either deposited directly onto pre-patterned devices [3, 8] or plasma etched from a bulk graphene-insulator-substrate stack [4, 7]. For both configurations, a current is passed through the conducting graphene channel when a voltage drop is created across the source and drain electrodes. Sweeping the back-gate voltage modulates the charge carrier contributions in the graphene channel producing distinctive transfer curve characteristics [9]. Recombination events between the target analytes and the immobilized bioreceptors on the graphene surface can be transduced to a measurable signals via changes in the graphene's electronic properties. Graphene's compatibility with existing planar CMOS manufacturing processes [9] combined with its ease of functionality [2] and high sensitivity will facilitate these low-cost devices as truly disruptive biosensing technologies in the future.

The widespread existence of the heavy metal lead in the environment is a significant threat to the health of humans. Ever since the industrial revolution, lead's proliferation into a variety of products has caused an epidemic in exposure. Moreover, combining its continuous use in a myriad of industrial settings with its non-biodegradability has resulted in an ever-increasing accumulation of this chemical in the environment [10]. Lead is a neurotoxin that accumulates over time in the body restricting the cognitive, behavioral and psychological development of children [11]. Specifically, one way in which the lead ion (Pb^{2+}) has shown to impede cognition is its action as an effective interfering agent against calcium ions which drive ion channels in animal cells [10]. Lead in drinking water is an issue that particularly harms children as not only do they absorb between four to five times more per oral dose than adults do [12] but both their internal and external tissues being softer than adults make them more susceptible to damage [10]. Additionally, their under-developed blood-brain barriers allow for easier lead penetration into the brain [11]. Most of the current techniques for lead detection require highly skilled personnel using expensive, complex and centralized lab-based equipment for their work [13]. There is a need for the development of low-cost, sensitive and portable devices to facilitate the widespread testing of Pb^{2+}, in order that exposure to this ion via common routes like drinking water sources is reduced.

This work exploits aptamers as specific bioreceptors immobilized to the surface of the graphene channel for the detection of Pb^{2+}. Aptamers are small chains of nucleotides (oligonucleotides) in the form of single stranded RNA or DNA which have folded and have the ability to interact with target analytes. These oligonucleotides are produced using the Systematic Evolution of Ligands by Exponential Enrichment (SELEX) technique. Briefly, this process starts when a large pool of random RNA/DNA chains are incubated with the desired target. The chains that bind often fold to form complexes with the target. Unbound oligonucleotides are removed from the pool before bound RNA/DNA chains are amplified by Polymerase Chain Reaction (PCR). Further RNA/DNA chains are produced from the outputs of the PCR process, with a higher affinity for the target, which are subsequently re-introduced into the selection pool. These stages are then repeated, usually between 5-15 times, before the oligonucleotides are sequenced, identified and characterized. The resulting oligonucleotides are highly specific for the target analyte [14, 15].

Aptamers offer several advantages over antibodies in their use as bioreceptors and have continued to attract significant interest in the bio-sensing field. Aptamers offer greater stability over antibodies as they are able to recover their structure after heating, unlike antibodies whose conformation is easily denatured at high temperatures. Batch to batch variation in performance from antibodies produced in mammalian cell cultures is avoided for Aptamers due to their repeatable manufacturing process, which also offers the possibility of chemical modifications which can aid down-stream conjugation procedures [16].

A popular bioreceptor for the detection of lead ions in modern techniques is the Thrombin Binding Aptamer (TBA) [17, 18]. TBA (5'-GGTTGG TGT GGTTGG-3') is a 15 base, single stranded, DNA oligonucleotide. TBA is rich in the guanine nucleotide base and therefore is susceptible to folding into G-quartet/G-quadruplex structures. These

structures are formed when a quartet of guanine nucleotide bases are assembled into a planar structure bonded together by specialist Hoogsteen hydrogen bonds [19]. Cations stabilize these structures when they position themselves within the plane or between planes of the G-quartets. It is conjectured that a contributing factor of lead's toxicity and therefore damage to humans is caused by this stabilizing influence it has on genetic material [20]. The selectivity of TBA towards Pb^{2+} over other interfering ions Li^{+}, Na^{+}, Mg^{2+}, Ca^{2+}, Cu^{2+}, Co^{2+}, Ni^{2+}, Zn^{2+}, Cd^{2+}, Cr^{3+}, Al^{3+}, Fe^{3+} and Au^{3+} has been demonstrated by Liu's group who exploited the phenomenon of fluorescence resonance energy transfer (FRET) in order to transduce Pb^{2+} binding [18].

Herein GFET biosensors have been developed which harness TBA aptamers for the sensitive detection of Pb^{2+} ions. The immobilization of the TBA is conducted in two ways to evaluate how the indirect and direct immobilization strategies impact the sensing metrics.

2. Materials and Methods

2.1 Materials

Ultrapure de-ionized water (DIW) used throughout this work for buffer solutions and rinsing stages was obtained from a Purelab water purification systems with a resistivity value of 18.2 MΩcm. 1-pyrenebutyric acid N-hydroxysuccinimide ester (PBASE) was purchased from Sigma-Aldrich. A 1 x PBS solution, with pH of 7.4 was created by combining 1 PBS tablet (Fisher Scientific) with 100 mL of ultrapure DIW. These two were mixed with a magnetic stirrer to ensure adequate mixing. Analytical grade dimethylformamide (DMF) was purchased from Sigma Aldrich.

TBA oligonucleotides (hereafter oligos) with an amino-modified 5′ end were purchased from Eurofins Genomics. TBA oligos with a pyrene-tagged 5′ end (PTBA) were purchased from Metabion. Both oligos were ordered with a synthesis scale of 1 μmol and HPLC purification.

Four inch wafers of monolayer graphene on SiO_2/n^{++} type-Si were purchased from Graphenea. Lift-off resist 3B (LOR) was purchased from (Supplier-Micro Chem) The S1805 G2 positive photoresist (PR) and 1165 remover chemicals were purchased from (Supplier-Microposit).

2.2 Sensor Fabrication

2.2.1 Channel Shaping

GFET fabrication followed the process detailed in [4]. Channel shaping begins with spin-coating square chips of the graphene/SiO_2 wafer with LOR at 3000 rpm for 30 s followed by a baking stage in an oven at 175 ^{0}C for 15 min. The next step involved spin-coating PR at 3000 rpm for 30 s before soft-baking on a hotplate at 100 ^{0}C for 1 min. Standard photolithographic techniques were used to pattern the graphene channels (width 80 μm and length 720 μm) before the wafer underwent deep UV (DUV) treatment. DUV has shown to not only harden the remaining PR but also remove additional chemical residues on the wafer surface, which is discussed in more detail here [7]. Plasma etching was performed using Argon at 50 W for 2.5 min at a pressure of 10^{-6} torr. Three heat shrinks between the back of the wafer and the substrate holder were used along with the LOR in the first step to ensure that it was possible to remove all residue of PR after the plasma etching. This was performed by immersing the chips in remover heated to 60 ^{0}C for 1 h followed by room temperature for 14 h. The remover is washed away in DIW and the chips were then dried using an N_2 gun and stored in a vacuum chamber at 25-30 mmHg (33 mbar) for 1 hour. An overview of this process is given in Figure 1.

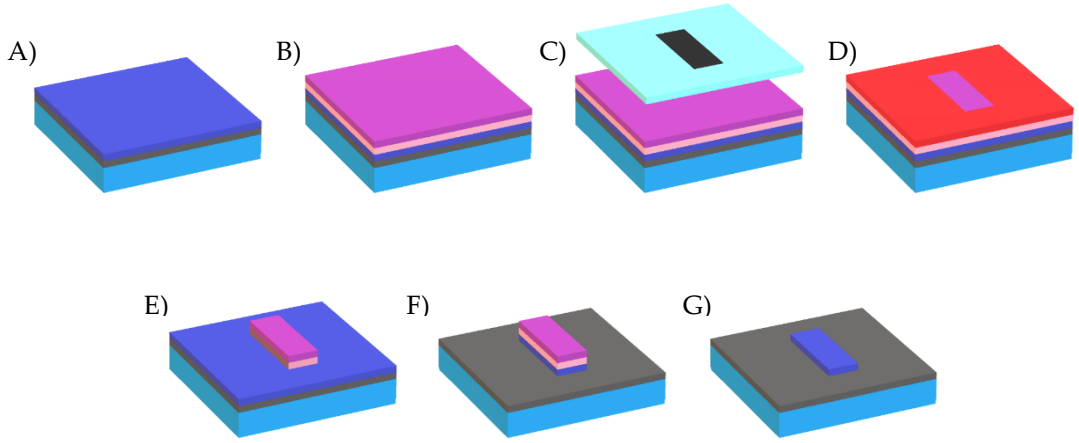

Figure 1. Shaping graphene channels overview A) Si (P++), SiO_2, Graphene stack, B) LOR and PR deposited onto graphene surface, C) Shield mask used to prevent UV ray transmission, D) Exposed PR and LOR are denatured by exposure of UV, E) Stack is developed which removes denatured PR and LOR, F) Plasma etching removes all graphene that is not protected by a PR and LOR stack, G) PR and LOR stack is removed from graphene channels by use of remover leaving shaped graphene channels.

2.2.2 Electrode Deposition

Depositing contacts over the shaped graphene channels begins with a similar photolithography process mentioned previously. The thermal evaporation of a Cr adhesive layer was performed at a current of 21 mA at a pressure of 10^{-6} torr for a total of 8 s to produce a layer ~5 nm thick onto the graphene and SiO_2 stack. A layer of ~30 nm of Au was sputtered onto the Cr at 250 W for 30 min at a pressure of 10^{-7} torr before a final removal stage is conducted. The shielding technique discussed in [21] was used to maximize device yield during the sputtering process. An overview of this process is given in Figure 2.

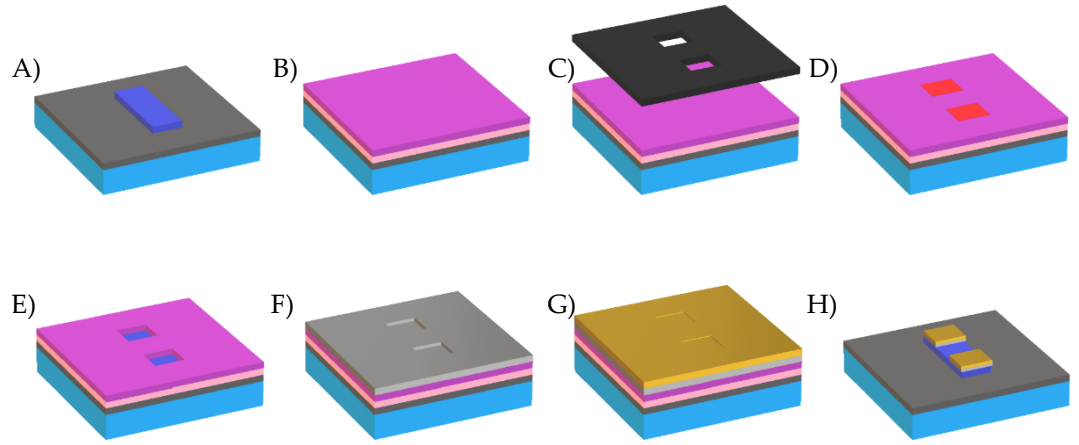

Figure 2. Electrode deposition overview A) Si (P++), SiO_2, Graphene stack after channel shaping, B) LOR and PR deposited on surface, C) Window mask used to allow UV ray transmission, D) Exposed PR and LOR are denatured by exposure of UV, E) Stack is developed which removes denatured PR and LOR leaving windows onto graphene surface, F) Cr is evaporated onto the surface, G) Au is sputtered onto the surface, H) PR and LOR coating is removed from surface by use of remover.

2.2 Conjugation Techniques

2.2.2 PBASE immobilization

Non-covalent functionalization of carbon nanotubes and graphene can be achieved by using the bi-functional molecule PBASE [22]. This form of functionalization is preferred for biosensing purposes for two primary reasons; firstly, the sp^2 hybridization in the lattice is preserved which maintains graphene's electronic characteristics and secondly it prevents the introduction of defects in the graphene lattice which are responsible for increasing the occurrence of non-specific detection at molecular adsorption sites [22, 23]. Figure 4A shows a schematic of PBASE which consists of two distinct ends, a highly aromatic pyrene group which binds to the Basal plane of graphene by π-π stacking and a highly reactive succinimidyl ester group which binds easily to amines via nucleophilic substitution [22].

The immobilization technique involved soaking the devices in a 10 mM PBASE solution (in DMF) for 4 h at room temperature. PBASE molecules which were not covalently bound to the graphene were removed by a rinse cycle in DMF and DIW before being dried using a N_2 gun.

2.2.3 Aptamer immobilization

One possible secondary structure that TBA forms as a bioreceptor immobilized on the surface of graphene is illustrated in Figure 3B and is predicted using the Mfold server [24]. Aptamers were immobilized in one of two ways in this work; indirectly (two-stage) and directly (one-stage), an overview of these processes is depicted from Figure 3C through D. Prior to conjugating aptamers, the indirect method relies on the successful formation of the PBASE self-assembly layer onto the graphene surface. Once this is achieved amino-modified TBA (Figure 3C top panel), which has previously undergone phosphoramidate chemistry to tag an amino group to the end of the oligo via a carbon 6 spacer, can then be used [25]. These aptamers are cross-linked to the NHS ester group via nucleophilic substitution to immobilize them to the surface of graphene (Figure 4D top panel).

The direct method for aptamer immobilization requires the use of pyrene-tagged TBA. As illustrated in Figure 3C bottom panel, one simple way of achieving this is by incubating amino-modified aptamers with PBASE. This facile technique has been used by Khan's group in their work on organic solvent-free aptamer functionalization of GFETs where they estimated 50%-90% binding efficiency using this method, based on details provided from their supplier [26]. Once the TBA have achieved conjugation with the pyrene group they can be bound directly to the graphene surface via π-π stacking without requiring pre-treatment of channel.

In practice, ~1 μL of 10 μM solution of amino-modified TBA/PTBA is drop-casted onto the GFET for the indirect and direct techniques. Both techniques relied on leaving their respective solutions to incubate on the surface of the GFET device at room temperature for 4 h in a humid environment to prevent solvent evaporation. Subsequently, a rinse cycle in the appropriate solvent and then DIW was conducted before a drying stage using N_2.

2.3 Characterization Techniques

2.3.1 Electrical Measurements

GFET devices were designed in an adapted Hall-bar configuration with multiple contact electrodes across the channel allowing the characterization of multiple individual sensors. The dimensions of the individual sensors are 80 μm wide by 95 μm long and are pictured in Figure 4A. This design allows four probe measurements to be conducted removing the resistance of the test leads.

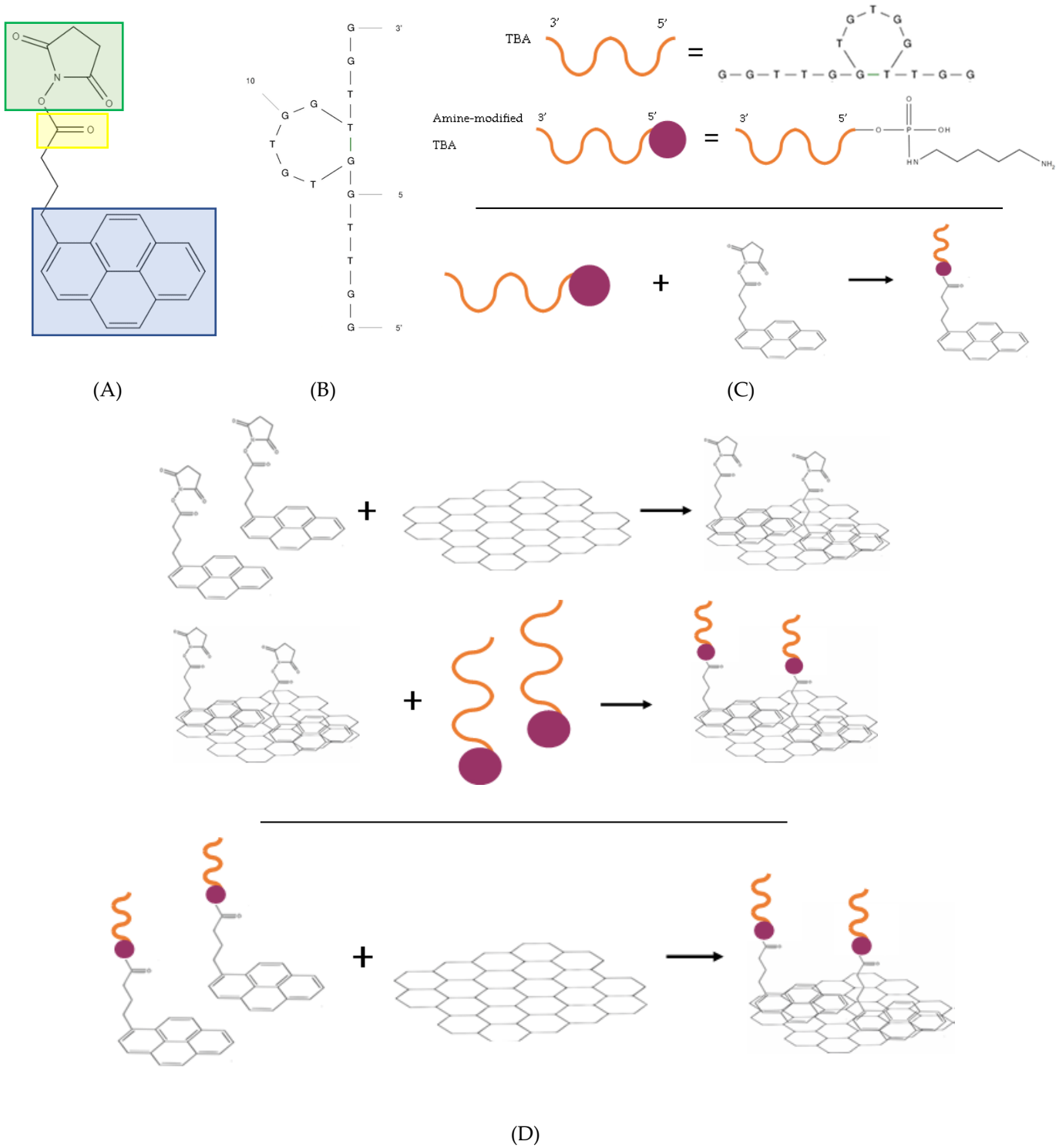

Figure 3. A) PBASE bi-functional molecule with pyrenyl, carbonyl and succinimidyl groups highlighted with the blue yellow and green boxes respectively. **B)** Mfold secondary structure prediction for TBA aptamers [24] **C)** Functional DNA preparation with Top Panel – Showing amino-modified (C6) 5′ end of TBA, Bottom Panel – Showing pyrene-tagged 5′ end of TBA. **D)** Conjugation pathways: Top Panel – Indirect, showing two stage process of conjugating PBASE to graphene initially followed by amino-modified DNA. Bottom Panel – Direct, showing pyrene-tagged TBA directly conjugated to graphene surface.

Electrical characterization consisted of both linear voltage (I_{SD}-V_{SD}) and back-gated voltage (I_{SD}-V_G) sweep measurements. During linear voltage sweep measurements the source-drain voltage (V_{SD}) was swept from -5 mV to +5 mV in 1 mV steps with the current through the channel recorded.

I_{SD}-V_G measurements were obtained by maintaining the V_{SD} at a constant +5 mV and sweeping the back-gate voltage forward from -100 V to +100 V and back again. Hysteretic behavior, shown by the difference in voltage and current for V_{DP}^F, V_{DP}^R is observed for most sensors and is caused by trapped charges between the graphene and the SiO_2 layer screening the influence of the applied electric field during each sweep direction [27]. A measurement schematic and typical I_{SD}-V_G measurement is pictured in Figure 4B and C respectively. The charge neutral points which correspond to the points of minimum conductivity in the channel for the forward and reverse sweeps are referred to as Dirac Points (V_{DP}^F, V_{DP}^R respectively). The mobility of the GFET is described by hole and electron conduction, referring to which charge carrier is the majority contributor to the current through the graphene channel at a particular V_G. At the Dirac point, the voltage of minimum conductance, the Fermi level sits at the intercept between the valence (majority hole) and conduction (majority electron) bands. Conduction in regions below (above) the Dirac point voltage show majority hole (electron) charge carrier contributions [9]. All measurements were taken using a Cascade Microtech (MPS150) Probe Station to facilitate four-probe measurements interfaced with a Keysight B1500A Semiconductor Device Analyzer (SDA) in the ambient lab environment.

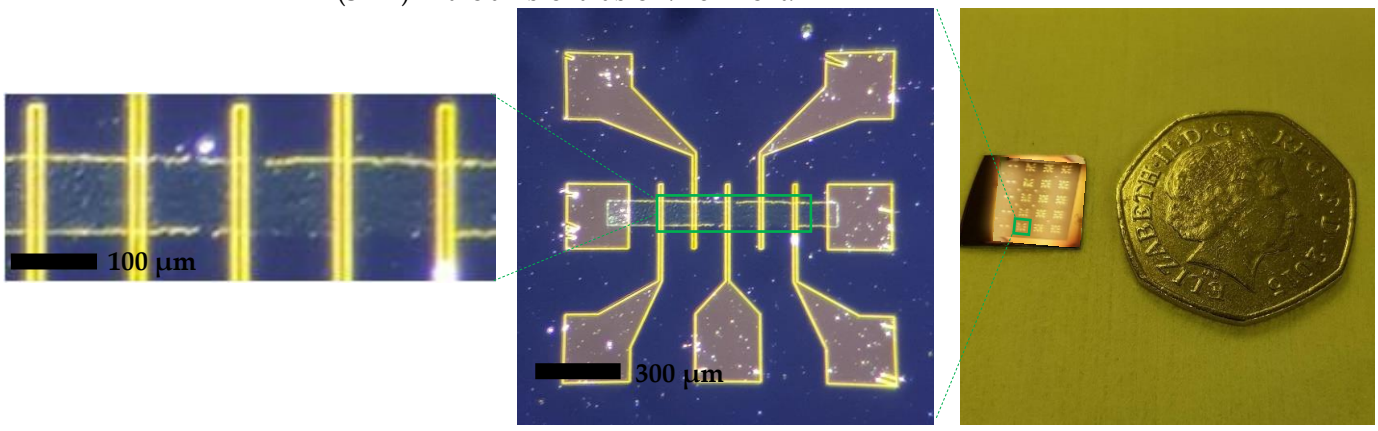

(A)

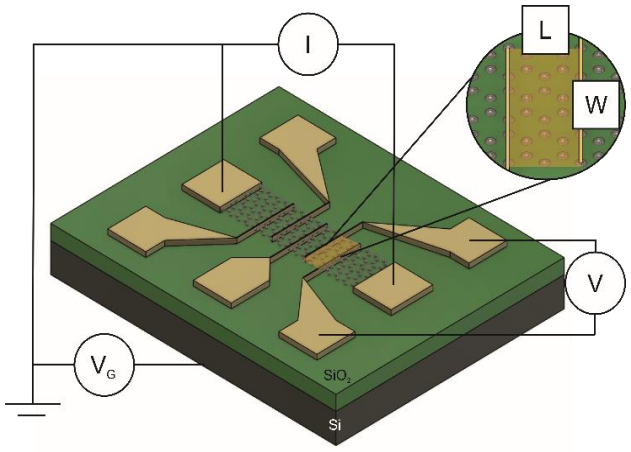

(B)

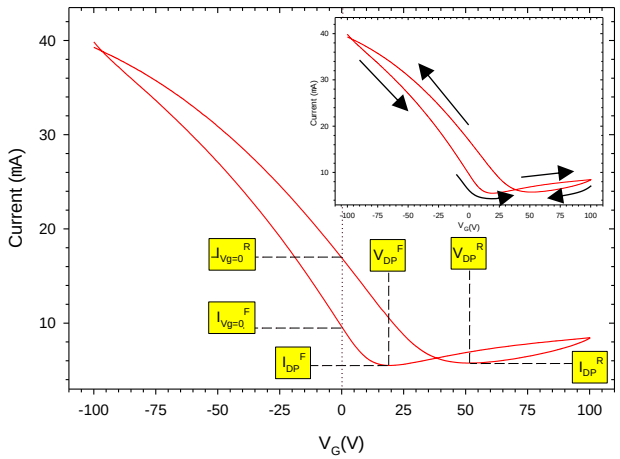

(C)

Figure 4. A) Left Panel – Individual sensors between electrodes across GFET device, Centre Panel - Typical 7-electrode GFET device, Right Panel – Fabricated chip at the end of the electrode deposition phase which consists of 20 devices with

50 pence coin for scale **B)** I_{SD}-V_G measurement **s**chematic showing four probe measurements with inset showing the convention for describing the width and length of channel used when calculating the field effect mobility. **C)** Typical I_{SD}-V_G sweep measurement showing positions of V_{DP}^F, V_{DP}^R, $I_{Vg=0}^F$, $I_{Vg=0}^R$, I_{DP}^F and I_{DP}^R with inset showing arrows which indicate the forward and reverse sweep directions.

Data analysis of the transfer curve characteristics of the GFETs was initially conducted in the SCRAMBLE software package [28]. This open-source and customizable software has been designed to facilitate the rapid processing of GFET transfer curves. For forward and reverse sweeps, SCRAMBLE automatically determines the Dirac points, positions of maximum transconductance and calculates the field effect mobilities for electrons and holes.

The field effect mobility is calculated in the SCRAMBLE software using the direct transconductance method (DTM) described in more detail in [29]. This method relates the mobility of the device (1) with the transconductance (2) and the back-gate capacitance (3).

$$\mu_{DTM} = g_m \frac{L}{W V_{SD} C_G} \quad (1)$$

$$g_m = \frac{\partial I_{SD}}{\partial V_G} \quad (2)$$

$$C_G = \frac{\varepsilon_r \varepsilon_0}{t_{ox}} \quad (3)$$

where μ is the field effect mobility, g_m is the transconductance, C_G is the back-gate capacitance, L, W are the length and width of the device respectively, V_{DS} is the source-drain voltage, ε_r is the relative permittivity (SiO_2), ε_0 is the permittivity of free space and t_{ox} is the thickness of the insulating SiO_2 layer.

2.3.2 Raman Measurements

Raman spectra of the graphene channel was measured using a Horiba XPLORA system with a 532 nm laser. A grating with 1200 gmm^{-1} groove density was chosen in order to reach a spectral resolution of roughly 2.8 cm^{-1} between 1000 cm^{-1} and 3000 cm^{-1} as recommended in [30]. For each functionalization stage, 25 individual Raman spectra were captured in a 5 x 5 grid to make a representative summary plot. This is necessary due to variations observed across Raman spectra within a graphene sample usually attributed with remnants of PMMA from the graphene transfer process [31]. All Raman measurements were conducted in the ambient lab environment with a laser power of ~4 mW.

2.3.3 Detection of Pb^{2+}

GFET devices were firstly conjugated with either TBA or PTBA aptamers. Once this was complete GFETs were exposed to increasing concentrations of Pb^{2+} ions. Specific amounts of Pb^{2+} ions were dissolved in DIW at concentrations of 1 nM, 10 nM and 100 nM. A 0.5 μL drop of a specific concentration of Pb^{2+} ions was pipetted directly onto the device and left to incubate in an ambient environment for ~10 min. This time frame was sufficient to achieve solvent evaporation from the device surface allowing electrical characterization to take place in dry conditions. Once dry, every sensor on the GFET device was then electrically characterized in order to improve the reliability of results.

3. Results and Discussion

3.1 Characterisation of PBASE treated graphene

Figure 5A shows the Raman spectrum for fabricated graphene and graphene treated with 10 mM PBASE in DMF. Successful conjugation of the PBASE to the graphene surface is indicated by the additional peaks introduced after treatment. The new peaks at ~1212 cm^{-1} and ~1402 cm^{-1} are associated with the presence of pyrene groups and have been observed in [32, 33] as evidence of binding. The hybridization of orbitals between

the pyrene base interacting with the graphene lattice is responsible for the ~1362 cm^{-1} peak whilst the additional shoulder at ~1611 cm^{-1} is a result of the pyrene group resonating due to the π-π stacking interaction [34].

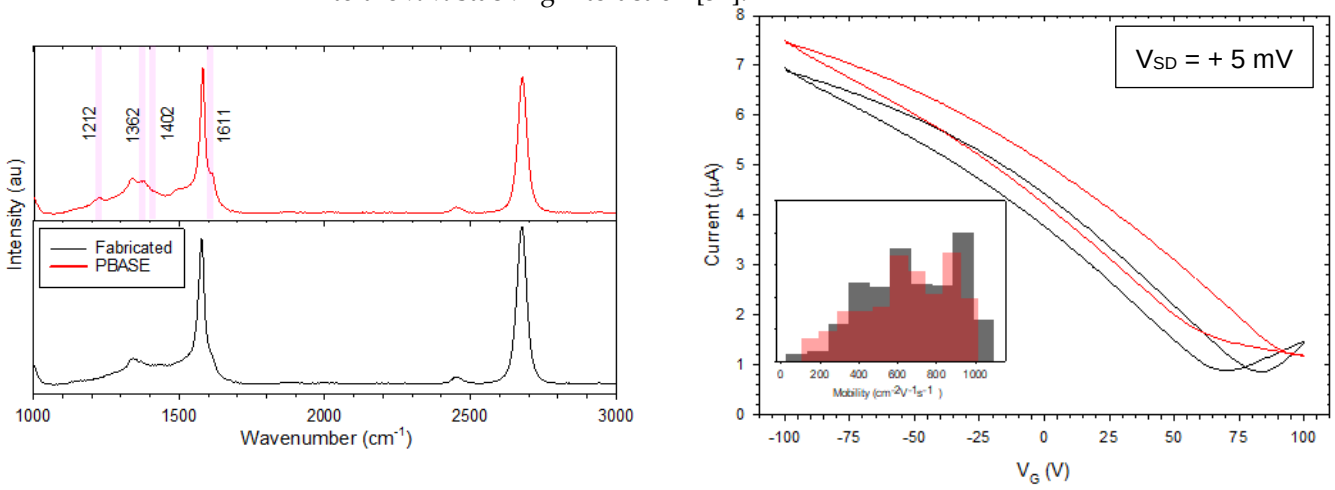

(A) (B)

Figure 5. A) Typical Raman spectra of fabricated graphene (black) and graphene treated with 10 mM PBASE (red). Additional peaks introduced as a result of conjugation are highlighted with the pink regions. **B)** Typical I_{SD}-V_G measurement with inset showing the mobility values across the transfer curve.

The electrical characterization of fabricated graphene and graphene treated with 10 mM PBASE in DMF is shown in Figure 5B. The conjugation of PBASE has increased the position of the V_{DF} and V_{DR} to greater than + 100 V. A right shifting in this position is well documented in the literature [3, 35-38] and infers an increase in the density of hole charge carriers. The existence of an electron acceptor, in the form of PBASE's carbonyl group can be partially credited for this effect [31]. Interestingly, since the gradient of both transfer curves are similar throughout, the doping of the channel has not severely impacted the mobility of the charge carriers as displayed by the histogram plot in the inset of Figure 5B. It can be inferred by the lack of change exhibited in this observation that the non-covalent π-π stacking has been successful and has not negatively impacted the graphene's conductive properties [37]

3.2 Characterisation of aptamer functionalised graphene

As part of the initial characterization of the TBA and PTBA, UV-Vis was captured and are displayed in Figure 6A and B respectively. A strong peak in the absorbance at 260 nm for both complexes indicates the presence of DNA. Additional peaks shown in Figure 6B at ~280 nm, ~333 nm and ~345 nm are attributed to the pyrene group modification [39] and have been observed by Wang in [40] in similar experimental circumstances.

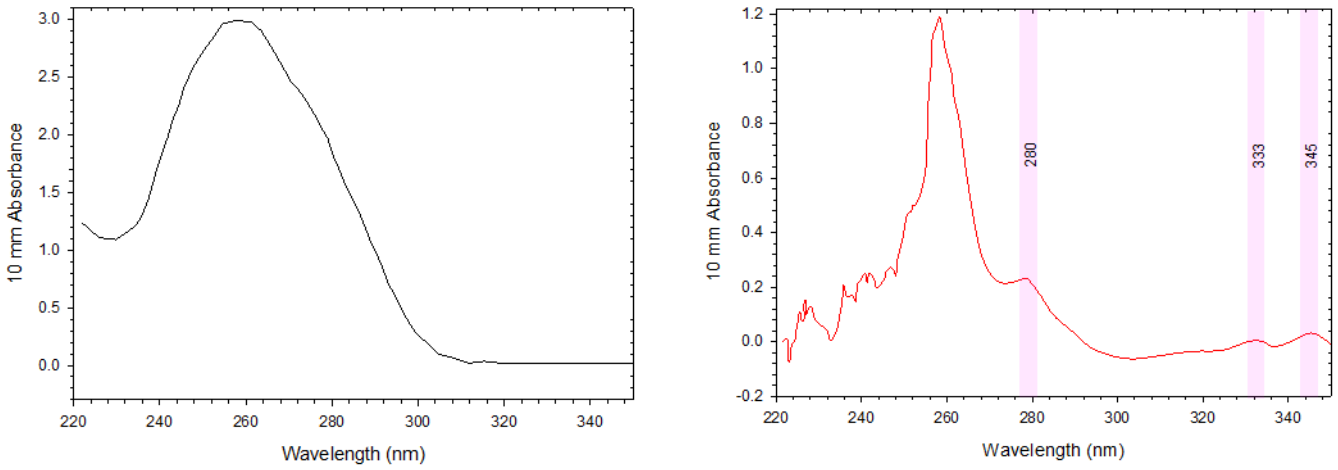

Figure 6. UV-Vis spectra of **A)** TBA **B)** PTBA with the additional peaks associated with pyrene group modification indicated in the pink shaded regions.

3.2.1 Indirect immobilization of TBA

Raman measurements were conducted on graphene after TBA was immobilised. As shown in Figure 7, there are no additional peaks caused by the immobilisation of TBA. This is supported by similar measurements conducted by Nekrasov's group [6]. The absence of an increase in the D peak highlights that this process does not increase the disorder and density of defects in the channel. This result is expected since the amine-modified TBA binds only to the active succinimidyl ester group of the PBASE molecule and not directly to the graphene channel.

The Raman measurements captured can still be used to infer the presence of TBA from the change in I(2D):I(G) ratio. Figure 7B plots the I(2D):I(G) against the I(2D):I(D) ratios for individual spectra captured at each of the functionalization stages. It has been shown that ratio between I(2D):I(G) can be used to describe the doping of the graphene channel, with a negative correlation observed between I(2D):I(G) and doping [41]. It is observed from Figure 7 that there is clear clustering between the functionalization stages. Since the metrics are bunched together in this manner it shows good repeatability in the data collected at each stage. Next, it is clear that as the functionalization has progressed the I(2D):I(G) ratio has decreased, firstly from fabricated to PBASE and then from PBASE to TBA treated graphene. This indicates an increase in the doping of the channel at each step caused by the immobilized structures. Finally the I(2D):I(D) ratio follows the same pattern. The initial reduction in this metric comes from an increase in the D peak caused by the increase in disorder that occurs due to the conjugation of PBASE. The reduction in this ratio during the TBA immobilization is caused by the reduction in the intensity of the 2D peak which is clearly visible in Figure 7A.

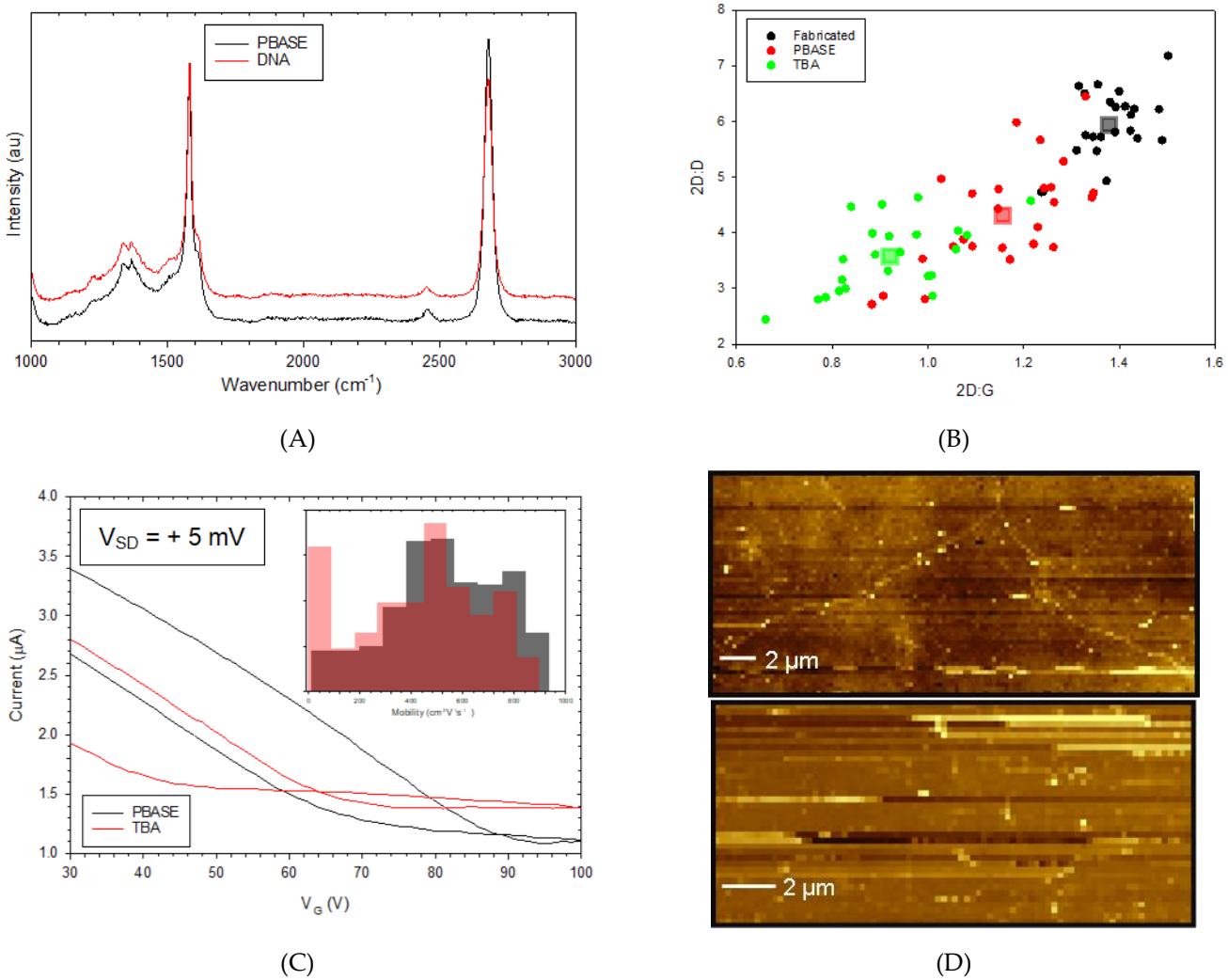

Figure 7. A) Typical normalised Raman spectrum of graphene after 10 mM PBASE immobilisation (black line) and 10 μM TBA immobilisation (red line) with offset applied for clearer graphical visualisation **B)** Scatter plot showing evolution of I(2D):I(G) and I(2D):I(D) ratios for fabricated (black), 10 mM PBASE (red) and 10 μM TBA (green) functionalized graphene with average values indicated by square markers. **C)** Typical I_{SD}-V_G measurement of GFET sensor treated with 10 μM TBA (red) compared to PBASE treated graphene (black) with inset showing calculated mobility values. **D)** Surface topology of graphene channel examined by atomic force comparison (AFM). Top Panel - Fabricated graphene Bottom Panel – TBA/PBASE functionalized graphene.

The transfer curve presented in Figure 7C shows a clear left shifting in V_{DP^R}, from +95 V to +81 V caused by the electron donation from the DNA. This left shifting effect is in agreement with the observations made by Chee et al who used a similar guanine rich aptamer for their work on Pb^{2+} ion detection [42]. The peak mobility values are similar between the two as depicted by the histogram plot in the inset of Figure 7C indicating that the graphene lattice remains unchanged and therefore its sensitive electronic structure remains intact after binding, as desired from the non-covalent functionalization using the PBASE layer. AFM measurements shown in Figure 7D were used to confirm TBA binding which can be inferred by the 420% and 662% increase in RMS and Mean roughness respectively caused by the TBA/PBASE immobilization.

3.2.2 Direct immobilization of TBA

A comparison of the Raman measurements was conducted after completing the direct immobilization of PTDA and are shown across Figure 8. The existence of the additional ~1616 cm^{-1} shoulder peak was present in some sample positions captured across the

25 point map. This peak, associated with pyrene group resonating with the graphene lattice due to the π-π stacking interaction provides evidence of binding. However, caution should be applied against relying solely on this metric to confirm successful binding of the PTDA to the graphene since this peak is also associated with surface charges and impurities and can be present in untreated graphene as displayed in Figure 7A [43]. To further strengthen the evidence supporting PTDA functionalization in this work, further analysis into the Raman spectra are presented. This analysis was derived from measurements across 25 individual spots. Firstly, enhanced doping of the graphene channel is indicated by the decrease in the I(2D):I(G) ratio shown in Figure 7B as previously discussed. Next, left shifting of the PP(2D) specifically infers the doping of graphene by electrons, donated by the conjugated electron rich aptamers [44, 45].

AFM measurements shown in Figure 8D were used to confirm TBA binding which can be inferred by the 227% and 375% increase in RMS and Mean roughness respectively caused by the PTBA oligos.

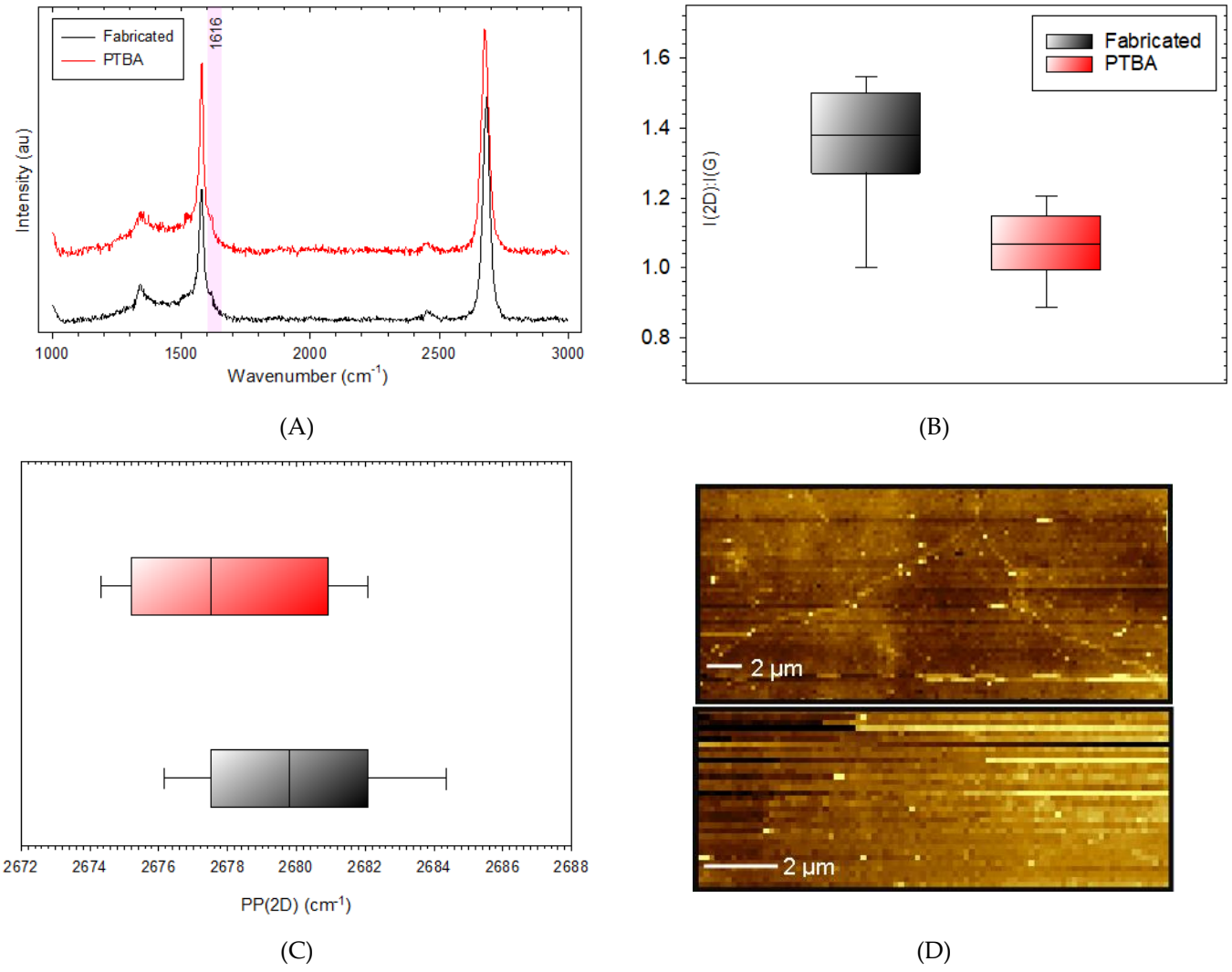

Figure 8. A) Single spot Raman spectra of fabricated graphene (black) and PTBA functionalised (red) with presence of the ~1616 shoulder peak highlighted with pink region. Box and whisker plots for typical fabricated (black) and PTDA functionalized (red) graphene for **B)** I(2D):I(G) and **C)** PP(2D) **D)** Surface topology of graphene channel examined by AFM. Top Panel - Fabricated graphene and Bottom Panel - PTBA functionalized graphene.

3.3 Sensing Characteristics of Pb^{2+} ions using GFET sensors

In the work presented here GFET devices were functionalized using both the indirect and direct strategies for the detection of Pb^{2+} ions in order to produce a direct comparison between the two techniques at the same bioreceptor concentration of 10 μM. Multiple GFET devices, each with several individual sensors were measured at every functionalization step in order to improve reliability of results. It was necessary to normalize the device responses in order that inter-device variations were eliminated. This was achieved by calculating a ratio of the response against that measured at the previous TBA/PTBA stages. An example of this calculation for $I_{Vg=0}$ is given in Equation 4 below.

$$\boldsymbol{R_{Vg=0}} = \frac{\boldsymbol{I_{Vg=0}^{Pb^{2+}}}}{\boldsymbol{I_{Vg=0}^{TBA/PTBA}}} \quad (4)$$

The standard error was subsequently calculated in order to plot error bars across the results which detail the spread in data across sensors.

3.3.1 Indirect immobilization of TBA

The detection of Pb^{2+} ions was initially conducted using the indirect immobilization of TBA. This detection method was applied to a total of 12 sensors across 3 GFET devices. Large variation was observed across these different sensors using this technique with no repeatable correlation in metrics against Pb^{2+} concentration.

An example of two very different sensor responses are shown in Figure 8A and B and correspond to sensors D1 and D2 respectively. The transfer curves for D1 and D2 differ significantly across all the sensing stages. For D1 there are no clear Dirac points within the -/+ 100 V range when the Pb^{2+} ions are added as indicated by Figure 8A. On the other hand, when the Pb^{2+} ions were added to sensor D2, the Dirac points are clearly visible. Moreover, these Dirac points are observed as left shifting with increasing concentration of Pb^{2+} ions as indicated by the inset of Figure 8B.

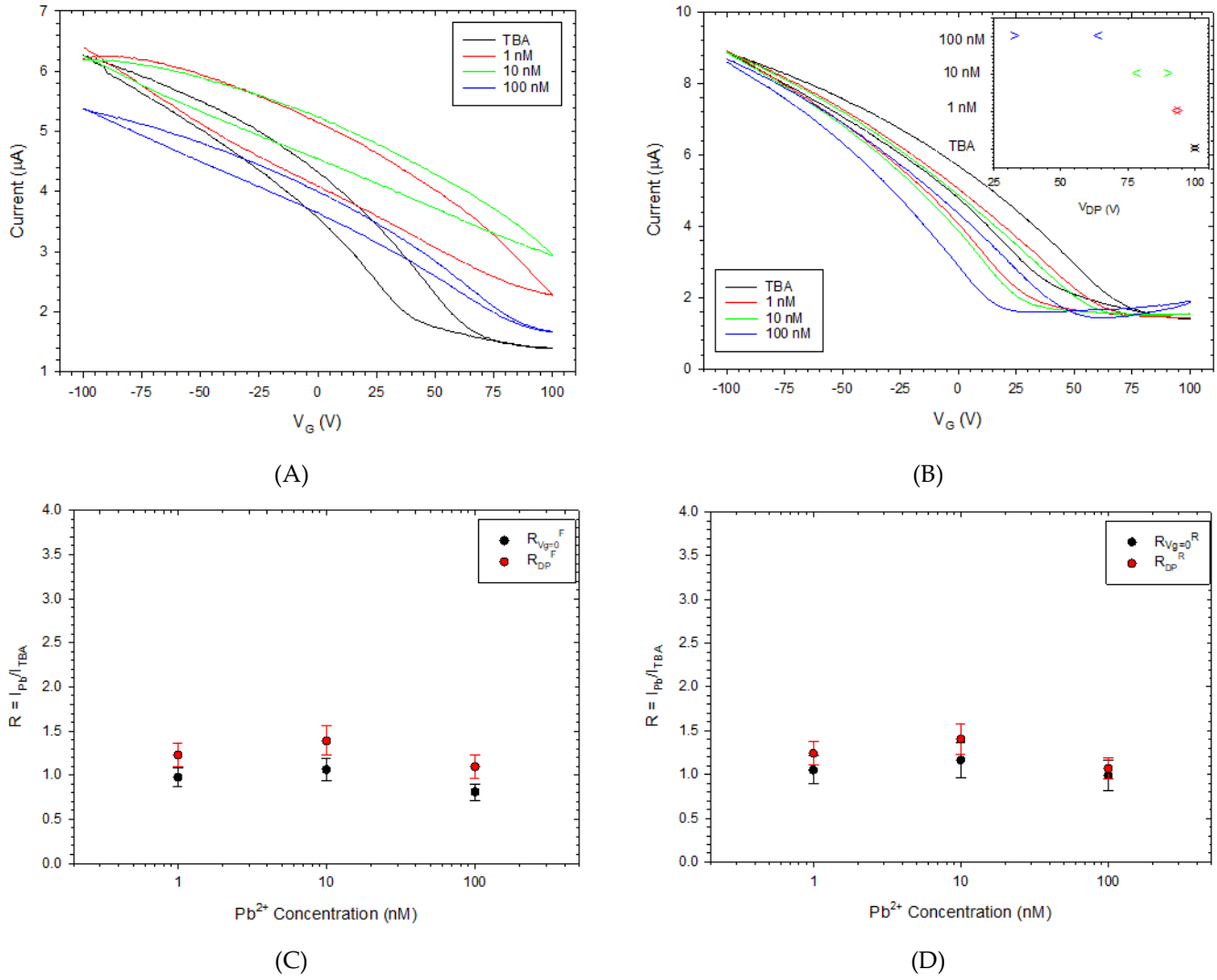

Figure 9. Transfer curves of TBA functionalised GFET sensor on exposure to Pb^{2+} ions at increasing concentrations for **A)** D1 and **B)** D2 sensors with inset showing left shifting in the V_{DP} with increasing Pb^{2+} concentration. Normalised values against logarithm of Pb^{2+} concentration showing current metrics across Pb^{2+} range of 1 nM to 100 nM for **C)** $I_{Vg=0}{}^{F}$ and $I_{DP}{}^{F}$ **D)** $I_{Vg=0}{}^{R}$ and $I_{DP}{}^{R}$

Decreasing values of V_{DP}^{F} and V_{DP}^{R} with increasing Pb^{2+} concentrations can be explained with the following mechanism. As the Pb^{2+} ions bind to the TBA they cause the strands to undergo conformational changes into G-quadruplex structures. The impact of these structures is to bring the nucleotide bases closer to the graphene surface. This simulates an increasing DNA concentration that is observed by the channel which has the result of n-doping the graphene caused by the interaction between the lattice and the electron-rich nucleotide bases as also observed by Chen et al [46]. With ever more G-quadraplex structures forming on the surface in line with an increasing in Pb^{2+} concentration this causes further n-doping and thus enhanced left shifting of the Dirac points. Although this negative shift aligns with the proposed sensing scheme this observation only occurred on 25% of the sensors tested. Clearly improved repeatability is required in order that a higher confidence can be made with these results.

The shift in metrics relating to $I_{Vg=0}^{F}$, I_{DP}^{F}, $I_{Vg=0}^{R}$ and I_{DP}^{R} are shown in Figure 8B and C. These metrics combine the results of the 12 sensors in order to improve reliability and have been normalized against the TBA stage in order to eliminate variations between sensors. It is observed that there is no correlation in these metrics against Pb^{2+} concentration.

3.3.1 Direct immobilization of TBA

Unlike for the indirect method, the direct method showed improved repeatability across the sensors. This detection method was applied to a total of 6 sensors across 3 GFET devices. Transfer curves for a typical GFET sensor exposed to increasing Pb^{2+} concentration used in this work are shown in Figure 10A. The shift in metrics relating to $I_{Vg=0}^{F}$, I_{DP}^{F}, $I_{Vg=0}^{R}$ and I_{DP}^{R} are shown in Figure 10B and C. These metrics combine the results of the 6 sensors in order to improve reliability and have been normalized against the PTBA stage in order to eliminate variations between sensors. It is shown that $I_{Vg=0}^{F}$, I_{DP}^{F}, $I_{Vg=0}^{R}$ and I_{DP}^{R} all decrease with increasing Pb^{2+} concentration. An exponential relationship between these metrics and the concentration of Pb^{2+} is indicated by the best fit line plotted in Figure 10B and C.

The decrease in the metrics relating to current can be ascribed to the impact of doping. As shown in Figure 10A the PTBA functionalized sensors exhibit only p-type charge carrier conduction. Prior to any binding events with Pb^{2+} ions the PTDA aptamers are flexible and take on a structural shape as proposed earlier in Figure 3B. When the Pb^{2+} ions combine with the PTBA, they form G-quadraplex structures causing the aptamers conformation to change into a more closely folded shape [26]. This change in structure encourages electron donation between the electron-rich nucleotide bases and lattice causing a decrease in the hole carrier density thus decreasing the current through the channel [46]. Since the positions of the V_{DP}^{F} and V_{DP}^{R} lie outside the detectable range for all sensors (as depicted in Figure 10A) it is not possible to confirm that this effect causes a negative shift in the Dirac points.

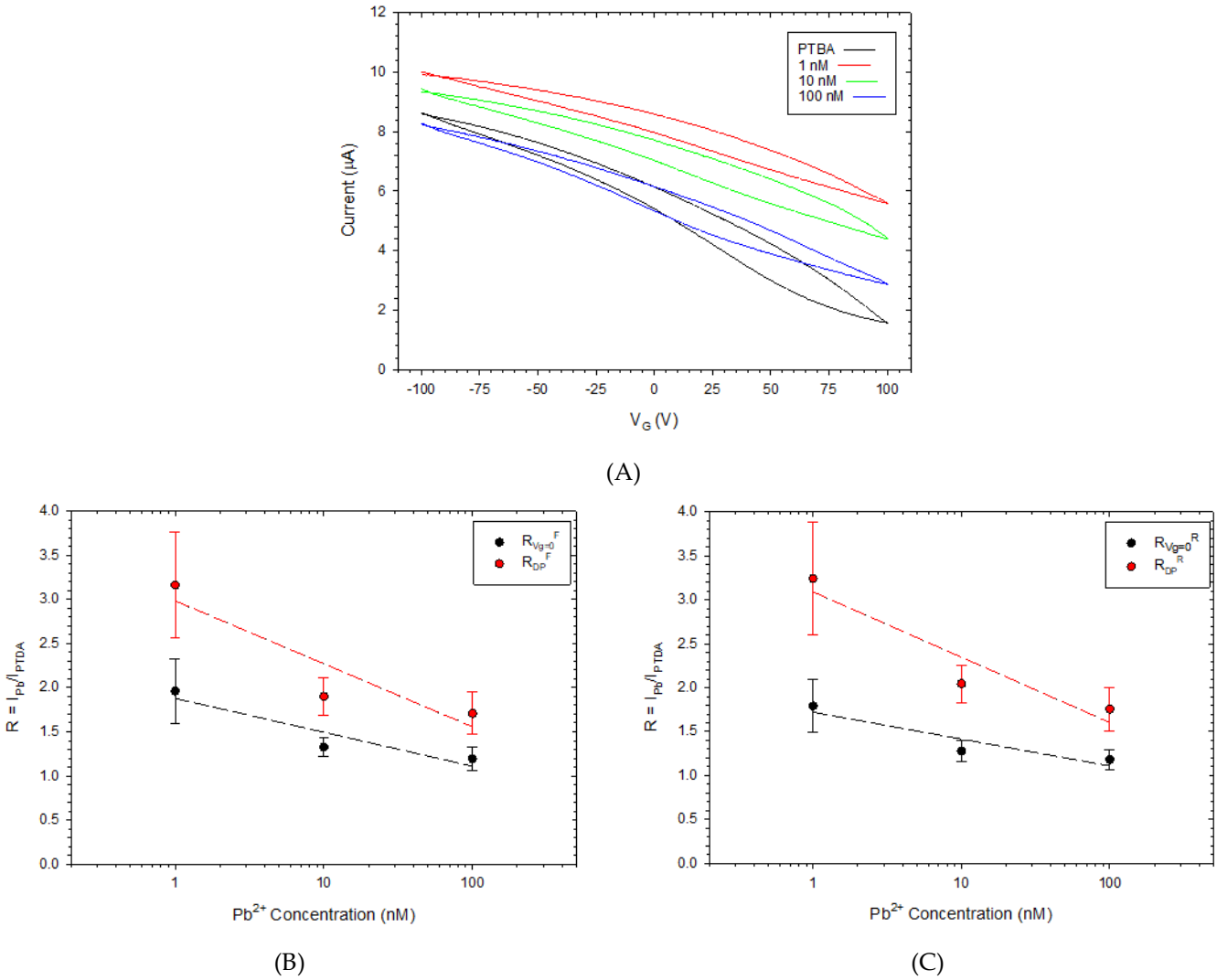

Figure 10. A) Typical transfer curves of PTBA functionalized GFET sensors on exposure to Pb^{2+} ions at increasing concentrations. Normalized values against logarithm of Pb^{2+} concentration showing decrease in metrics across Pb^{2+} range of 1 nM to 100 nM for **B)** $I_{Vg=0}{}^F$ and $I_{DP}{}^F$ **C)** $I_{Vg=0}{}^R$ and $I_{DP}{}^R$.

The initial results shown in Figure 10B and C show the response of the GFET devices (via the direct immobilisation of 10 μM PTBA oligos) to increasing Pb^{2+} ion concentrations in DIW. Although there is some evidence of an enhanced discrimination between these concentration levels, more experiments are required in order that the analytical performance of these devices can be improved. Specifically, it would be advantageous to optimise the signal differences between concentrations whilst decreasing the noise.

It was not possible to confirm targeted Pb^{2+} ion detection using sensors immobilised with 10 μM TBA oligos using the indirect method as the response remains close to 1 across all current metrics for these initial results. One possible explanation for the difference observed between the two techniques is the interplay between the PBASE layer, immobilised at a concentration of 10 mM and the TBA nucleotides, conjugated at a concentration of 10 μM. Perhaps the higher density of PBASE molecules prevents the TBA nucleotides from forming the G-quadraplex structures consistently. Future work will focus on the optimisation of the PBASE and TBA concentration levels.

Both techniques would benefit from the removal of atmospheric adsorbents prior to functionalization. It is well documented that graphene's characteristics change on exposure to the ambient environment [45, 47, 48]. Removing such contaminants on graphene's

surface would bring the starting V_{DP} closer to the $V_G = 0$ value so that future shifts would remain within the detectable -/+100 V range. This would allow a more comprehensive study of the change in electronic characteristics by tracking the shift in V_{DP}. Possible strategies for achieving this involve vacuum desorption [47], rapid thermal annealing [49] and electrochemical cleaning [50] which have all shown to reduce doping and bring V_{DP} closer to 0 V.

Ongoing improvements to this work will involve testing the sensors' response to interfering agents, such as $Cu^{2+}$and Fe^{3+}which are commonly found ions found in DIW. One way this could be optimised is by exploiting surface passivation techniques such as the use of Ethanolamine and Bovine Serum Albumim.

4. Conclusions

GFET devices functionalized directly with PTBA oligos were demonstrated in this work to detect Pb^{2+} ions. Raman, electrical and AFM characterization was conducted throughout the functionalization stages to confirm successful conjugation of the bioreceptors. The sensing mechanism detailed in this work relies on the conformational change of the immobilized TBA oligos on binding with individual Pb^{2+} ions into G-quadraplex structures. This compact form encourages electron donation to the graphene lattice from the electron rich nucleotides bases. This acted to decrease the density of majority hole charge carriers in the channel which is transduced as a reduction in measured current. The direct immobilization strategy showed good repeatability and is completed in one step. Combined with a scalable fabrication process detailed herein, it is envisioned that this technique can provide low-cost and rapid sensors suitable for the detection of Pb^{2+} ions in drinking water sources thus limiting humans' exposure to the toxin. Further investigations are required to optimize the sensing strategy when TBA is immobilized to the graphene surface via the PBASE linker.

Author Contributions: Conceptualization, B.O.D; methodology, B.O.D., V.R. and T.B.; software, B.O.D.; validation, B.O.D.; formal analysis, B.O.D. and V.R.; data curation, B.O.D. and V.R.; writing—original draft preparation, B.O.D.; writing—review and editing, All; visualization, B.O.D. and V.R.; supervision, T.W., S.A.A. and P.D. ; project administration, S.A.A.; funding acquisition, S.A.A, V.R. and S.S.G. All authors have read and agreed to the published version of the manuscript.

Funding: We acknowledge funding from the University of Plymouth GD110025-104 and the Global Challenges Research Fund (GCRF), Project code: SP/GCRF-19/003.

Conflicts of Interest: The authors declare no conflict of interest.

References

1. K. S. Novoselov, et al., *Electric Field Effect in Atomically Thin Carbon Films.* Science, 2004. **306**.
2. Novoselov, K.S., et al., *A roadmap for graphene.* Nature, 2012. **490**(7419): p. 192-200.
3. Ping, J., et al., *Scalable Production of High-Sensitivity, Label-Free DNA Biosensors Based on Back-Gated Graphene Field Effect Transistors.* ACS Nano, 2016. **10**(9): p. 8700-8704.
4. Haslam, C., et al., *Label-Free Sensors Based on Graphene Field-Effect Transistors for the Detection of Human Chorionic Gonadotropin Cancer Risk Biomarker.* Diagnostics (Basel), 2018. **8**(1).
5. Bungon, T., et al., *Graphene FET Sensors for Alzheimer's Disease Protein Biomarker Clusterin Detection.* Frontiers in Molecular Biosciences, 2021. **8**(188).
6. Nekrasov, N., et al., *Graphene-Based Sensing Platform for On-Chip Ochratoxin A Detection.* Toxins (Basel), 2019. **11**(10).
7. Suhail, A., et al., *Reduction of polymer residue on wet–transferred CVD graphene surface by deep UV exposure.* Applied Physics Letters, 2017. **110**(18): p. 183103.

8. Kakatkar, A., et al., *Detection of DNA and poly-l-lysine using CVD graphene-channel FET biosensors.* Nanotechnology, 2015. **26**(12): p. 125502.
9. Reddy, D., et al., *Graphene field-effect transistors.* Journal of Physics D: Applied Physics, 2012. **45**(1).
10. Wani, A.L., A. Ara, and J.A. Usmani, *Lead toxicity: a review.* Interdisciplinary toxicology, 2015. **8**(2): p. 55-64.
11. Hou, S., et al., *A clinical study of the effects of lead poisoning on the intelligence and neurobehavioral abilities of children.* Theoretical biology & medical modelling, 2013. **10**: p. 13-13.
12. Hanna-Attisha, M., et al., *Elevated Blood Lead Levels in Children Associated With the Flint Drinking Water Crisis: A Spatial Analysis of Risk and Public Health Response.* American journal of public health, 2016. **106**(2): p. 283-290.
13. Zhou, G., et al., *Real-Time, Selective Detection of Pb2+ in Water Using a Reduced Graphene Oxide/Gold Nanoparticle Field-Effect Transistor Device.* ACS Applied Materials & Interfaces, 2014. **6**(21): p. 19235-19241.
14. Schütze, T., et al., *Probing the SELEX Process with Next-Generation Sequencing.* PLOS ONE, 2011. **6**(12): p. e29604.
15. Komarova, N. and A. Kuznetsov, *Inside the Black Box: What Makes SELEX Better?* Molecules, 2019. **24**(19): p. 3598.
16. Song, K.-M., S. Lee, and C. Ban, *Aptamers and Their Biological Applications.* Sensors, 2012. **12**(1).
17. Xu, K., et al., *Graphene- and aptamer-based electrochemical biosensor.* Nanotechnology, 2014. **25**(20): p. 8.
18. Liu, C.-W., C.-C. Huang, and H.-T. Chang, *Highly Selective DNA-Based Sensor for Lead(II) and Mercury(II) Ions.* Analytical Chemistry, 2009. **81**(6): p. 2383-2387.
19. Rosu, F., et al., *Tetramolecular G-quadruplex formation pathways studied by electrospray mass spectrometry.* Nucleic acids research, 2010. **38**(15): p. 5217-5225.
20. Liu, W., et al., *Kinetics and Mechanism of Conformational Changes in a G-Quadruplex of Thrombin-Binding Aptamer Induced by Pb2+.* The Journal of Physical Chemistry B, 2011. **115**(44): p. 13051-13056.
21. Li, B., et al., *Shielding technique for deposition of Au electrical contacts on graphene by sputtering.* Journal of Vacuum Science & Technology A, 2015. **33**(3): p. 030601.
22. Chen, R.J., et al., *Noncovalent Sidewall Functionalization of Single-Walled Carbon Nanotubes for Protein Immobilization.* Journal of the American Chemical Society, 2001. **123**(16): p. 3838-3839.
23. Kim, D., et al., *Electrical conductance change of graphene-based devices upon surface modification for detecting botulinum neurotoxin.* Japanese Journal of Applied Physics, 2017. **56**(6).
24. Zuker, M., *Mfold web server for nucleic acid folding and hybridization prediction.* Nucleic Acids Research, 2003. **31**(13): p. 3406-3415.
25. Hermanson, G.T., *Bioconjugate Techniques*. 2008, Burlington, UNITED STATES: Elsevier Science & Technology.
26. Khan, N.I. and E. Song, *Detection of an IL-6 Biomarker Using a GFET Platform Developed with a Facile Organic Solvent-Free Aptamer Immobilization Approach.* Sensors, 2021. **21**(4).
27. Yang, J., et al., *Hysteresis analysis of graphene transistor under repeated test and gate voltage stress.* Journal of Semiconductors, 2014. **35**(9): p. 094003.
28. O'Driscoll, B., *SCRAMBLE: Sweep Comparison Research Application for Multiple Back-Gated FieLd Effect measurements of graphene field effect transistors.* SoftwareX, 2021. **15**: p. 100757.
29. Zhong, H., et al., *Comparison of mobility extraction methods based on field-effect measurements for graphene.* AIP Advances, 2015. **5**(5).
30. NPL, *Characterisation of the Structure of Graphene*, in *Good Practice Guides*, N.P. Laboratory, Editor. 2017, NPL.
31. Wu, G., et al., *Doping effects of surface functionalization on graphene with aromatic molecule and organic solvents.* Applied Surface Science, 2017. **425**: p. 713-721.
32. Li, Y., et al., *Fully integrated graphene electronic biosensor for label-free detection of lead (II) ion based on G-quadruplex structure-switching.* Biosensors and Bioelectronics, 2017. **89**: p. 758-763.

33. Fernandes, E., et al., *Functionalization of single-layer graphene for immunoassays.* Applied Surface Science, 2019. **480**: p. 709-716.
34. Liu, Y., et al., *Giant enhancement in vertical conductivity of stacked CVD graphene sheets by self-assembled molecular layers.* Nature Communications, 2014. **5**(1): p. 5461.
35. Wang, S., et al., *Graphene field-effect transistor biosensor for detection of biotin with ultrahigh sensitivity and specificity.* Biosensors and Bioelectronics, 2020. **165**: p. 112363.
36. Zhou, L., et al., *Label-free graphene biosensor targeting cancer molecules based on non-covalent modification.* Biosensors and Bioelectronics, 2017. **87**: p. 701-707.
37. Ono, T., et al., *Glycan-functionalized graphene-FETs toward selective detection of human-infectious avian influenza virus.* Japanese Journal of Applied Physics, 2017. **56**(3).
38. Seo, G., et al., *Rapid Detection of COVID-19 Causative Virus (SARS-CoV-2) in Human Nasopharyngeal Swab Specimens Using Field-Effect Transistor-Based Biosensor.* ACS Nano, 2020. **14**(4): p. 5135-5142.
39. Gao, Y., et al., *Solvent-dependent fluorescence property of multi-walled carbon nanotubes noncovalently functionalized by pyrene-derivatized polymer.* Nanotechnology, 2009. **20**(13): p. 135705.
40. Wang, C., et al., *A label-free and portable graphene FET aptasensor for children blood lead detection.* Sci Rep, 2016. **6**: p. 21711.
41. Das, A., et al., *Monitoring dopants by Raman scattering in an electrochemically top-gated graphene transistor.* Nat Nanotechnol, 2008. **3**(4): p. 210-5.
42. Chee, L.H., et al. *DNA/AuNP-graphene back-gated field effect transistor as a biosensor for lead (II) ion detection*. in *2017 IEEE Regional Symposium on Micro and Nanoelectronics (RSM)*. 2017.
43. Kwong Hong Tsang, D., et al., *Chemically Functionalised Graphene FET Biosensor for the Label-free Sensing of Exosomes.* Sci Rep, 2019. **9**(1): p. 13946.
44. Berciaud, S., et al., *Probing the Intrinsic Properties of Exfoliated Graphene: Raman Spectroscopy of Free-Standing Monolayers.* Nano Letters, 2009. **9**(1): p. 346-352.
45. Sojoudi, H., et al., *Impact of post-growth thermal annealing and environmental exposure on the unintentional doping of CVD graphene films.* Journal of Vacuum Science & Technology B, 2012. **30**(4): p. 041213.
46. Chen, T.-Y., et al., *Label-free detection of DNA hybridization using transistors based on CVD grown graphene.* Biosensors and Bioelectronics, 2013. **41**: p. 103-109.
47. Yang, Y., K. Brenner, and R. Murali, *The influence of atmosphere on electrical transport in graphene.* Carbon, 2012. **50**(5): p. 1727-1733.
48. Ni, Z.H., et al., *The effect of vacuum annealing on graphene.* Journal of Raman Spectroscopy, 2009. **41**(5): p. 479-483.
49. Jang, C.W., et al., *Rapid-thermal-annealing surface treatment for restoring the intrinsic properties of graphene field-effect transistors.* Nanotechnology, 2013. **24**(40): p. 405301.
50. Fu, W., et al., *Biosensing near the neutrality point of Graphene.* Science Advances, 2017. **3**: p. 7.